AJNR

Early Detection of Global Cerebral Anoxia: Improved Accuracy by High- *b*-Value Diffusion-Weighted Imaging with Long Echo Time

Khin K. Tha, Satoshi Terae, Toru Yamamoto, Kohsuke Kudo, Chihiro Takahashi, Masaki Oka, Shinji Uegaki and Kazuo Miyasaka

AJNR Am J Neuroradiol 2005, 26 (6) 1487-1497
http://www.ajnr.org/content/26/6/1487

Early Detection of Global Cerebral Anoxia: Improved Accuracy by High-*b*-Value Diffusion-Weighted Imaging with Long Echo Time

Khin K. Tha, Satoshi Terae, Toru Yamamoto, Kohsuke Kudo, Chihiro Takahashi, Masaki Oka, Shinji Uegaki, and Kazuo Miyasaka

BACKGROUND AND PURPOSE: **Early and accurate detection of global cerebral anoxia is important for determination of prognosis and further management. We evaluated whether accuracy in early detection of global cerebral anoxia was improved by high-*b*-value diffusion-weighted imaging (DWI) with long echo time (TE).**

METHODS: **Routine DWI (b = 1000 s/mm^2; TE = 139 ms), high-*b*-value DWI (b = 3000 s/mm^2; TE = 190 ms), T2-weighted imaging (T2WI), and fluid-attenuated inversion recovery (FLAIR) imaging were acquired in six patients who experienced cardiopulmonary arrest within 24 hours and six volunteers. Region of interest–based analysis was performed. Regions of interest of patients showing significant decrease in apparent diffusion coefficient (ADC) values than volunteers were considered abnormal. Three neuroradiologists independently assessed images of the patients for conspicuity of hyperintensity within regions of interest. Receiver operating characteristic (ROC) analysis was performed, and the area under the curve (*Az*) was compared among sequences and observers. Average contrast and contrast-to-noise ratios between abnormal regions of interest and regions of interest of normal surrounding parenchyma were calculated.**

RESULTS: **For all observers, high-*b*-value DWIs achieved the largest *Az*, and FLAIR imaging the lowest *Az*. *Az* of routine DWI and T2WI were between these values. High-*b*-value DWI and FLAIR imaging showed no significant interobserver variation in *Az*, whereas routine DWI and T2WI did. High-*b*-value DWI also achieved the largest contrast and contrast-to-noise ratios.**

CONCLUSION: **High-*b*-value DWI with long TE improved accuracy in early detection of global cerebral anoxia. Application of the sequence would facilitate early diagnosis.**

Several attempts are made to achieve early and accurate detection of global cerebral anoxia, because its presence and extensiveness influence prognosis and further clinical management (1–4). Among the currently developed techniques, diffusion-weighted imaging (DWI)—an MR imaging sequence—is known to allow detection of global cerebral anoxia early (ie, within 24 hours) within the acute period (1, 5). It enables early detection through its high sensitivity to restricted diffusion immediately following anoxic insult (1, 6). In the acute period, it shows restricted diffusion due to global cerebral anoxia as hyperintensity with decreased apparent diffusion coefficient (ADC) values, usually in cerebral cortex, deep gray matter, and cerebellum (1, 6).

Techniques that can improve accuracy in detection of global cerebral anoxia are desirable for more accurate determination of prognosis and management. Theoretically, high-*b*-value DWI can offer improved contrast between abnormal and normal tissues (7, 8). With improved contrast, improved accuracy in detection can be expected. There are, however, some potential disadvantages of high-*b*-value DWI, among which the reversal of gray-white matter contrast can limit accuracy in detection (7–10). One possible way to eliminate the reversal of gray-white matter contrast is through suppression of signal intensity from background brain parenchyma by using long echo times (TEs). In this study, we determined whether the high-*b*-value DWI with long TE (b = 3000 s/mm^2; TE = 190 ms) could improve accuracy in detection of the

Received August 9, 2004; accepted after revision November 4.

From the Departments of Radiology (K.K.T., S.T., K.K., C.T., M.O.), Health Sciences (T.Y.), and Emergency Services (S.U.), Hokkaido University Graduate School of Medicine, Sapporo, Japan.

Presentation at the 90th annual meeting of the Radiological Society of North America, Chicago, IL, November 30, 2004.

Address correspondence to Khin Khin Tha, Department of Radiology, Hokkaido University Graduate School of Medicine, N-15, W-7, Kita-ku, Sapporo, 060-8638, Japan.

TABLE 1: Demographic characteristics of the patients

Patient (no.)	Age (y)	Sex	Insult	Time to Restore Spontaneous Beating (min)	GCS at Admission	GCS at MRI	Interval between Insult and MRI (h)	Clinical Outcome
1	79	M	Choking	30	3	3	18.3	Vegetative state
2	20	M	Atrial fibrillation	30	3	3	21.9	Vegetative state
3	69	M	Ventricular fibrillation	33	4–6	4–6	3.8	Vegetative state
4	79	F	Choking	33	3	3	8.1	Vegetative state
5	54	M	Hanging	29	3	3	8.6	Vegetative state
6	25	F	Hanging	35	3	3	16.6	Deceased

Note.—GCS refers to Glasgow Coma Scale.

acute period of global cerebral anoxia, over routine DWI (b = 1000 s/mm^2; TE = 139 ms). T2-weighted imaging (T2WI) and fluid-attenuated inversion recovery (FLAIR) imaging, which may show signal intensity abnormalities (1, 4, 8), were also evaluated.

Methods

Study Population

The imaging data for this prospective study was collected over a 19-month period (from October 2001 through April 2003). The study included all patients who were admitted for histories of cardiopulmonary arrest and underwent MR examination within 24 hours from the anoxic insult. Six patients (four men and two women; age range, 20–79 years; mean age, 54.3 years) were eligible for the study. Demographic data of the patients, type of insult, the time taken to restore spontaneous beating, clinical status on hospital admission and MR examination, interval between the insult and MR examination, and clinical outcome are shown in Table 1. To determine the normal ADC values, MR studies were also obtained from six healthy volunteers (four men, two women; age range, 26–68 years; mean age, 47.1 years). The study was performed according to guidelines of the institutional review board, and informed consent for MR examination was obtained from families of the patients and all volunteers.

Imaging

All MR examinations were conducted on a 1.5-T MR imager, which is equipped with echo-planar imaging capabilities and can generate maximum gradient strength of 20 mT/m, slew rate of 125 T/m/s, and minimum rise time of 160 μs. The MR imaging protocol consisted of the routine DWI, high-b-value DWI, T2WI, and FLAIR imaging sequences. For all sequences, 19 5-mm-thick axial sections, parallel to the connection line between anterior and posterior commissures, were obtained. The interslice gap was 1.5 mm, and the field of view (FOV) was 240 mm × 240 mm. The matrix size in acquiring DWI was 128 × 128, interpolated into 256 × 256. The matrix sizes for T2WI and FLAIR imaging were 512 × 512 and 256 × 256, respectively.

A single-shot spin-echo echo-planar pulse sequence was used for DWI. The diffusion-encoding gradients were simultaneously activated along three orthogonal axes (X, Y, and Z) to generate trace DWIs. The high-b-value DWI was achieved through incrementation of gradient strength and duration. For each sequence, the echo-planar images with no diffusion weighting were also obtained, for use in image registration, placement of regions of interest, calculation of ADC and T2 values, and construction of signal intensity density curves. The repetition time (TR), TE, and total number of excitation (NEX) for routine DWI were 4,180 ms, 139 ms, and 2, and those for high-b-value DWI were 5510 ms, 190 ms, and 10, respectively. Total acquisition time for routine DWI was 33 seconds, and that for high-b-value DWI was 220 seconds.

The imaging parameters for T2WI and FLAIR imaging were as follows: TR = 4500 ms; effective TE = 105 ms; echo train length (ETL) = 7; NEX = 2, for T2WI; and TR = 9000 ms; TE = 104 ms; inversion time (TI) = 2500 ms; ETL = 11; NEX = 1, for FLAIR imaging. The total acquisition time for T2WI was 258 seconds, and that for FLAIR imaging was 200 seconds.

Generation of ADC Maps

The ADC maps were generated on a workstation, by using a two-point estimation technique. The ADC value (D) corresponding to each b value (b) was derived from the formula,

$$S(b) = S(0)e^{-bD}, \quad (1)$$

where $S(b)$ is the signal intensity of DW image at a given b value and $S(0)$ is the signal intensity at b value of 0 s/mm^2. To reduce error in calculation of ADC values, the DW images and echo-planar T2-weighted images were registered before generation of ADC maps. A commercially available software was used for the purpose.

Evaluation

To facilitate quantitative assessment, region of interest–based analysis was performed. Sixty-nine regions of interest, each measuring 4.7 mm × 4.7 mm, were placed at the left half of the brain of each patient or volunteer (Fig 1 and Table 2). Regions of interest were manually placed at each anatomic position on the echo-planar images with no diffusion weighting, T2-weighted images, and FLAIR images. In case of DWI, regions of interest, which were initially placed on the echo-planar images with no diffusion weighting, were directly superimposed. Care was taken to avoid inclusion of CSF and gross signal intensity heterogeneity in regions of interest. To maintain consistency, placement of all regions of interest was done by an author who did not take part in image interpretation.

ADC Values of Regions of Interest

The ADC values of regions of interest were measured. For each b value, regions of interest of the patients showing significant decrease in ADC values, compared with those of volunteers at corresponding locations ($P < .01$ by z test), were considered abnormal. Depending on the ADC values, regions of interest of the patients were divided into four groups: (1) regions of interest showing significant ADC decrease at both b values (abnormal regions of interest), (2) regions of interest showing no significant ADC decrease at both b values (normal regions of interest), (2) regions of interest showing significant ADC decrease only at b value of 3000 s/mm^2 (regions of interest abnormal only for b value of 3000 s/mm^2), and (4) regions of interest showing significant ADC decrease only at b value of 1000 s/mm^2 (regions of interest abnormal only for b

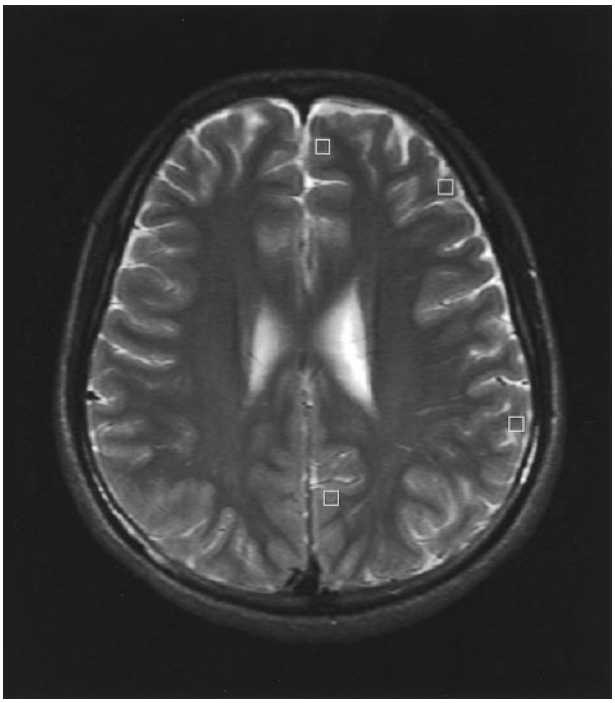

FIG 1. T2-weighted image of a patient, showing positions of regions of interest. The regions of interest are shown in square boxes (with white borders). The section shown contains four regions of interest. Regions of interest for other sequences are also set at the same positions.

TABLE 2: Regions of interest (ROIs) in each subject

Location	Total ROIs	
Frontal cortex	15	
Superior frontal gyrus		3
Middle frontal gyrus		3
Inferior frontal gyrus		3
Frontal part of cingulate gyrus		3
Precentral gyrus		3
Parietal cortex	15	
Postcentral gyrus		3
Insular cortex		3
Inferior parietal lobule		3
Precuneus		3
Parietal part of cingulate gyrus		3
Temporal cortex	15	
Superior temporal gyrus		3
Middle temporal gyrus		3
Inferior temporal gyrus		3
Hippocampus and uncus		3
Parahippocampal gyrus		3
Occipital cortex	6	
Cuneus		3
Lingual gyrus		3
Deep gray matter	6	
Corpus striatum		3
Thalamus		3
Pons	3	
Cerebellum	9	
Vermis		3
Superior to the great horizontal fissure		3
Inferior to the great horizontal fissure		3

value of 1000 s/mm^2). Only those regions of interest that achieved agreement of ADC results between the two *b* values (abnormal and normal regions of interest) were used in assessment of accuracy and calculation of average contrast and contrast-to-noise ratios.

Assessment of Accuracy in Detection of Signal Intensity Abnormalities

Three neuroradiologists (9–19 years experience), blinded to clinical information about the patients, independently assessed the images of patients for conspicuity of signal intensity abnormalities within regions of interest, by using a five-point confidence rating scale: 1 = definite absence of signal intensity abnormality; 2 = probable absence of signal intensity abnormality; 3 = indeterminate; 4 = probable presence of signal intensity abnormality; and 5 = definite presence of signal intensity abnormality. To minimize bias, image interpretation was done in four sessions, and an interval of 2 weeks was kept between sessions. Each session was arranged to contain all four sequences from six patients, but not more than single sequence per patient.

The receiver operating characteristic (ROC) analysis was performed for each sequence and observer, by using ROCKIT 0.9B software (C. E. Metz, University of Chicago). The ROC curves were calculated by plotting the true-positive fraction against likelihood of obtaining false-positive findings at each confidence level. The area under curve (*Az*) was obtained to compare diagnostic accuracy among sequences and observers. In addition to evaluation of overall *Az,* the *Az* value for each anatomic lobe (ie, frontal, parietal, temporal, or occipital lobe), deep gray matter (basal ganglia and thalami), brain stem, and cerebellum (including vermis) was also calculated. A univariate *z*-score test was used to determine statistical significance at 0.05.

Sensitivity, specificity, positive and negative predictive values of each sequence were evaluated by

$$2)\qquad Sensitivity = \frac{\text{Number of ROIs which showed significant ADC decrease and achieved positive rating } (>3)}{\text{Number of ROIs which showed significant ADC decrease}}$$

$$3)\qquad Specificity = \frac{\text{Number of ROIs which showed significant ADC decrease and achieved negative rating } (<3)}{\text{Number of ROIs which showed no significant ADC decrease}}$$

$$4)\qquad \text{Positive predictive value} = \frac{\text{Number of ROIs which showed significant ADC decrease and achieved positive rating } (>3)}{\text{Number of ROIs which achieved positive rating } (>3)}$$

$$5)\qquad \text{Negative predictive value} = \frac{\text{Number of ROIs which showed no significant ADC decrease and achieved negative rating } (<3)}{\text{Number of ROIs which achieved negative rating } (<3)}$$

Calculation of Average Contrast and Contrast-to-Noise Ratios

First, the contrast and contrast-to-noise ratios between the abnormal and normal regions of interest were calculated for each anatomic area.

The contrast ratio of each area was given by

$$6)\qquad (SI_l - SI_n)/(SI_l + SI_n),$$

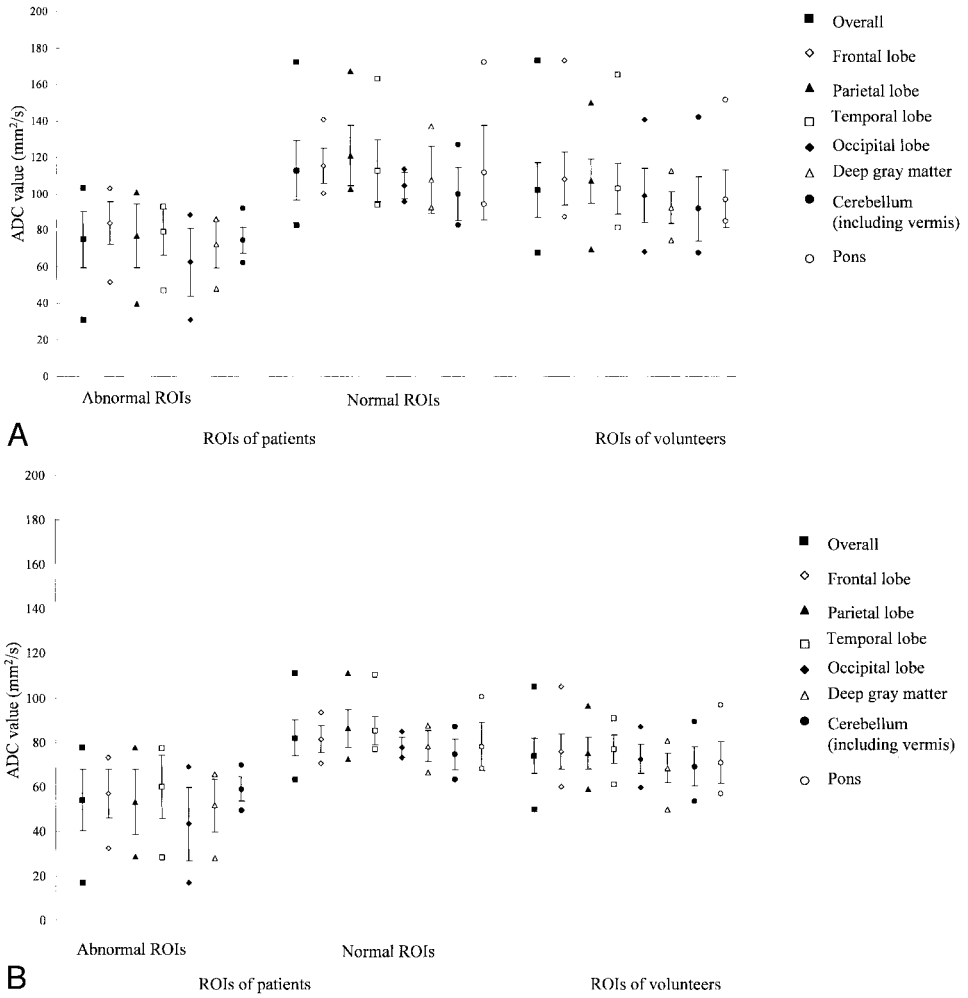

FIG 2. ADC values of abnormal and normal regions of interest of the patients, measurable at $b = 1000$ s/mm^2 (*A*) and at $b = 3000$ s/mm^2 (*B*). For each column, the uppermost point indicates the maximum ADC value. The middle point indicates the mean ADC value, and the lowermost point the minimum. The bars indicate SDs.

where SI_l is the average signal intensity of abnormal regions of interest and SI_n is the average signal intensity of normal regions of interest.

The contrast-to-noise ratio was given by

$$(SI_l - SI_n)/\sigma, \quad (7)$$

where σ is the average standard deviation of noise, measured as average standard deviation of 10 regions of interest placed somewhere within FOV, but outside the brain and free from artifacts.

Using the above ratios, the average contrast and contrast-to-noise ratios were then calculated. For both purposes, statistical significance between any two sequences was determined by paired *t* test, and the significance level was set as 0.05.

Calculation of T2 Value

To evaluate the influence of changes in T2, T2 values were calculated for all regions of interest. The two spin-echo echo-planar imaging sequences with no diffusion weighting (ie, the spin-echo echo-planar T2-weighted images obtained at TE = 139 ms and TE = 190 ms) were used in this calculation (11, 12). The T2 value (T2) of each region of interest was derived from

$$\frac{SI_a}{SI_b} = \frac{e^{-(139/T2)}}{e^{-(190/T2)}}, \quad (8)$$

where SI_a is the signal intensity of each region of interest at TE of 139 ms and SI_b is the signal intensity of the same region of interest at TE of 190 ms. The T2 values for each group of regions of interest of the patients were compared with those for normal volunteers. Unpaired *t* test was used to determine significance at 0.05.

Signal Intensity Attenuation Curves for DWIs

To observe the relationship between signal intensity attenuation on DWIs and *b* values, the natural logarithm of signal intensity ratio ($\ln S[b]/S[0]$) was plotted against *b* value (*b*). The curves for each group of regions of interest of the patients were compared with the curve for normal volunteers.

Estimation of Contrast-to-Noise Ratio and Az *Assuming Equal NEX*

To allow comparison of contrast-to-noise ratios between the two DWI sequences with different NEX, the contrast-to-noise ratio of high-*b* value DWI, assuming 2 NEX, was calculated.

Further, *Az* values of high-*b* value DWI with 2 NEX were estimated from the parameters of ROC curves on probability scale (13, 14). The *Y* intercept (α) and the slope (β) of ROC curves on probability scale for high-*b* value DWI with 10 NEX were determined first. The equations applied include

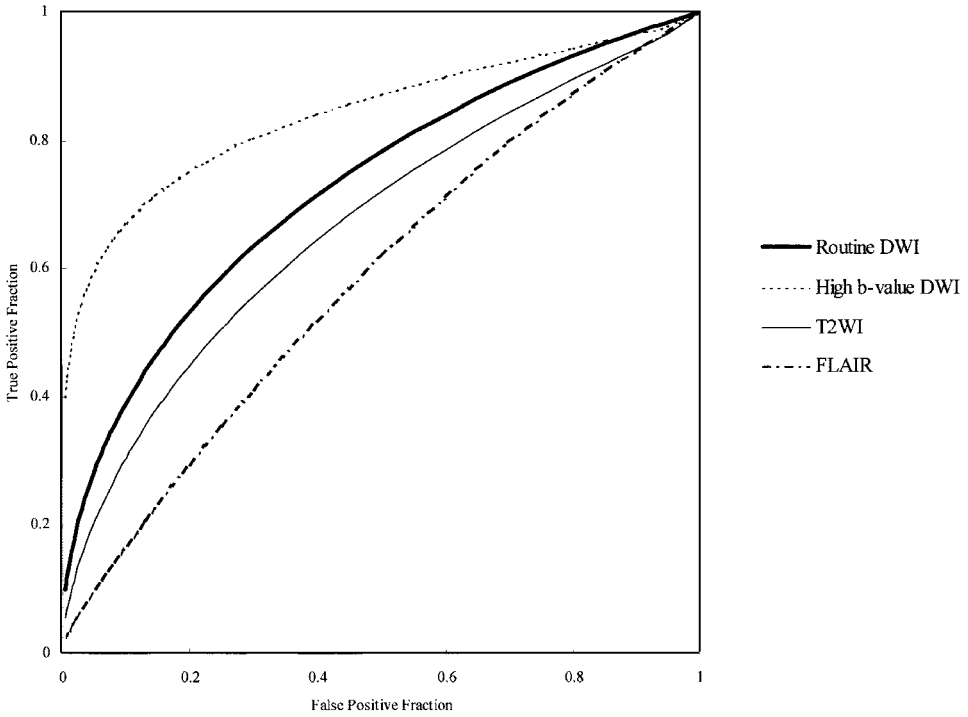

FIG 3. The ROC curves of each MR image achieved by the three observers. The high-*b*-value DWI holds the largest area under the curve (*Az*). The *Az* of the routine DWI (b = 1000 s/mm^2), T2WI, and FLAIR imaging follow in descending order.

9) $$\alpha = (SI_l - SI_n)/\sigma_l, \text{ and}$$

10) $$\beta = \sigma_n/\sigma_l,$$

where SI_l is the average signal intensity of abnormal regions of interest, SI_n is the average signal intensity of normal regions of interest, σ_l is the standard deviation of signal intensity distribution of abnormal regions of interest, and σ_n is the standard deviation of signal intensity distribution of normal regions of interest. σ_l and σ_n are given by,

11) $$\sigma_l = \sqrt{\sigma^2_{l0} + \sigma^2} \text{ and,}$$

12) $$\sigma_n = \sqrt{\sigma^2_{n0} + \sigma^2},$$

where σ_{l0} is the intrinsic standard deviation of signal intensity distribution of abnormal regions of interest, σ_{n0} is the intrinsic standard deviation of signal intensity distribution of normal regions of interest, and σ is the standard deviation of noise distribution which is proportional to NEX. When NEX decreases by one-fifth—ie, from 10 NEX to 2 NEX—σ_l and σ_n increase to $\sqrt{\sigma^2_l + 4\sigma^2}$ (ie, $\sqrt{\sigma^2_{l0} + 5\sigma^2}$) and $\sqrt{\sigma^2_n + 4\sigma^2}$ (ie, $\sqrt{\sigma^2_{n0} + 5\sigma^2}$). By using σ_l, σ_n, σ, and α and β of high-*b* value DWI with 10 NEX, α and β of high-*b*-value DWI with 2 NEX were estimated. Then, the *Az* value for high-*b*-value DWI with 2 NEX was calculated (13, 14).

Results

ADC Values of Regions of Interest

The total number of regions of interest in six patients was 414. The contributions of abnormal regions of interest and normal regions of interest were 164 (39.6%) and 155 (37.4%), respectively. The number of regions of interest abnormal only for *b* value of 3000 s/mm^2 was 29 (7.0%), and that for *b* value of 1000 s/mm^2 was 66 (15.9%). The ADC values of abnormal and normal regions of interest of patients and normal volunteers for each *b* value and anatomic area are shown in Fig 2.

Assessment of Accuracy in Detection of Signal Intensity Abnormalities

The ROC curves and the overall area under ROC curve (*Az*) achieved by each MR image are shown in Fig 3 and Fig 4. For all observers, the largest overall *Az* value was achieved by the high-*b* value DWI. For observer 1 and observer 3, the overall *Az* value achieved by high-*b* value DWI was followed by that of routine DWI, T2WI, and FLAIR imaging, in descending order. For observer 2, the overall *Az* value achieved by routine DWI was almost the same as that by T2WI. FLAIR imaging achieved the smallest overall *Az* value. The univariate *z* score test did not show any interobserver variation for the overall *Az* value of high-*b*-value DWI and FLAIR imaging. Interobserver disagreement, however, was noted for the overall *Az* value of the routine DWI and T2WI. High-*b*-value DWI also achieved the largest *Az* value for each anatomic area that could be evaluated (Table 3).

Sensitivity, specificity, positive and negative predictive values of each sequence are shown in Table 4. Sensitivity and positive and negative predictive values of high-*b*-value DWI were greater than any other sequences.

Figures 5 and 6 illustrate that the signal intensity abnormalities are more conspicuous on high-*b*-value DWI.

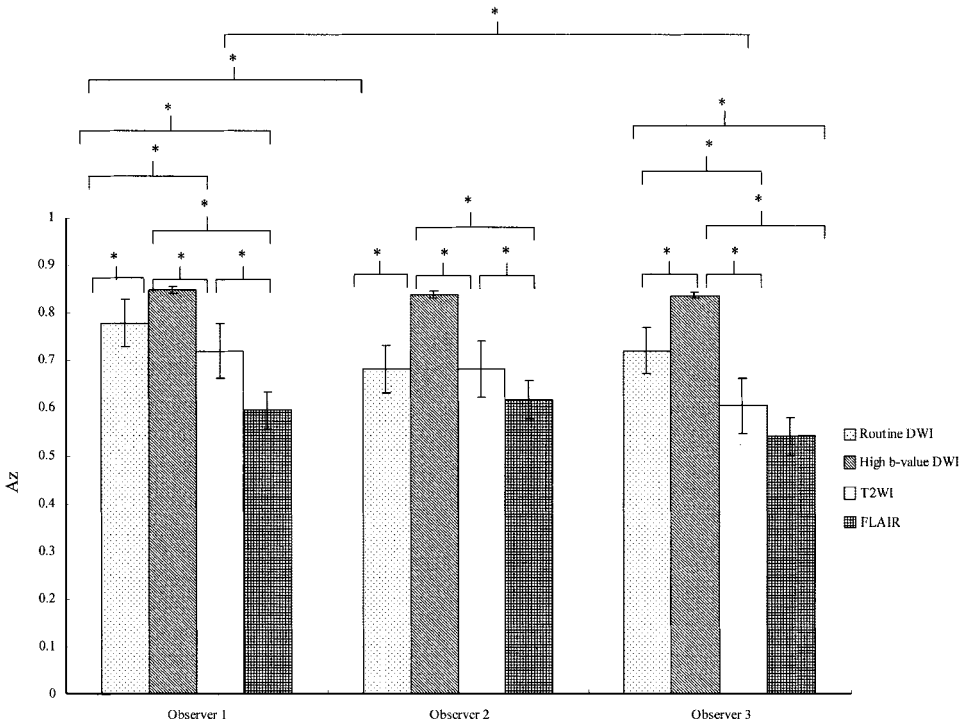

FIG 4. Histogram showing *Az* for each MR image and observer. Asterisk represents statistical significance ($P < .05$ by univariate *z* score test). For all observers, the high-*b*-value DWI achieves the largest *Az*. For observer 1, *Az* between any two sequences shows statistically significant difference. For observer 2, the statistically significant difference is noted between the high-*b*-value DWI or FLAIR images and any other sequences. No significant difference is observed between routine DWI and T2WI. For observer 3, statistically significant difference is noted between any two sequences, except for *Az* between T2WI and FLAIR imaging.

TABLE 3: The area under curve (Az) of each anatomical area

	Routine DWI	High-b-Value DWI	T2WI	FLAIR Imaging
Overall	0.73	0.84	0.67	0.58
Frontal lobe	0.72	0.81	0.59	0.57
Parietal lobe	0.67	0.89	0.65	0.60
Temporal lobe	0.67	0.69	0.55	0.55
Occipital lobe	*	*	*	*
Deep gray matter	0.79	0.90	0.70	0.44
Cerebellum	0.81	*	0.82	0.56

Note.—Asterisks represents degenerate data.

TABLE 4: Overall sensitivity, specificity, positive and negative predictive values of each sequence

	Routine DWI	High-b-Value DWI	T2WI	FLAIR Imaging
Sensitivity	0.66	0.74	0.44	0.27
Specificity	0.79	0.83	0.87	0.87
Positive predictive value	0.80	0.87	0.79	0.65
Negative predictive value	0.70	0.76	0.61	0.55

Calculation of Average Contrast and Contrast-to-Noise Ratios

The average contrast and contrast-to-noise ratios for each MR image are shown in Table 5.

The high-*b*-value DWI achieved significantly larger contrast ratio than any other sequences ($P < .05$). No statistically significant difference was noted among other sequences. The largest contrast-to-noise ratio was also achieved by high-*b*-value DWI. Statistically significant difference in contrast-to-noise ratio was noted between the high-*b*-value DWI and routine DWI or FLAIR imaging ($P < .05$). No statistically significant difference was noted among other sequences.

Calculation of T2 Value

Abnormal regions of interest and regions of interest abnormal only for *b* value of 1000 s/mm^2 revealed significant T2 shortening ($P < .05$; Table 6).

Signal Intensity Attenuation Curves for DWIs

The signal intensity attenuation curves are shown in Fig 7. The abnormal regions of interest showed least signal intensity attenuation. The curve for normal regions of interest was closest to that for normal volunteers. The distance between the curve for abnormal regions of interest and that for normal regions of interest was greater at high *b* value. The curves deviated from linearity with increasing *b* values, implying nonmonoexponential nature of signal intensity decay. The curve for regions of interest abnormal only at *b* value of 3000 s/mm^2 showed more marked deviation from linearity than that for regions of interest abnormal only at *b* value of 1000 s/mm^2. This curve approached that for normal volunteers at low *b* values but deviated upward at high *b* values. In contrast, the curve for regions of interest abnormal only

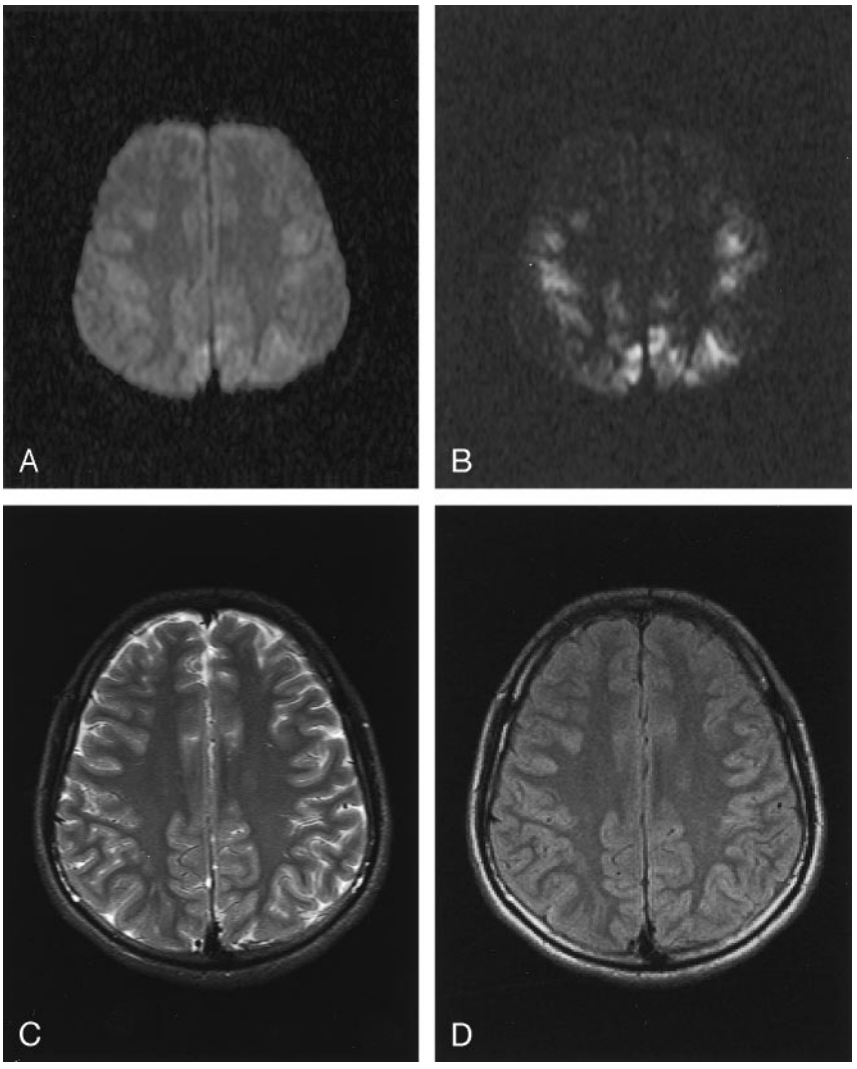

FIG 5. Routine DW image of a patient (*A*). High-*b*-value DW image (*B*). T2-weighted image (*C*). FLAIR image (*D*). The signal intensity abnormalities of bilateral cerebral cortex are more conspicuous on the high-*b*-value DWI.

at *b* value of 1000 s/mm^2 approached that for normal volunteers at high *b* values but ran farther away from it at low *b* values.

Estimation of Contrast-to-Noise Ratio and Az *Assuming Equal NEX*

The calculated contrast-to-noise ratio for high-b-value DWI with two NEX was $2.945/\sqrt{5} = 1.317$—ie, larger than that of routine DWI with equal NEX (1.112). The *Az* value of high-*b*-value DWI with 2 NEX was estimated as 0.76—ie, larger than the *Az* value of routine DWI (0.73).

Discussion

At high *b* values, the signal intensity from all tissues decline, depending on the ADC value (8). In principle, tissues with low ADC values suffer little signal intensity loss. Conversely, tissues with high ADC values experience pronounced signal intensity loss. This explains why the contrast and contrast-to-noise ratios between anoxic tissue (ie, tissue with very low ADC value) and surrounding normal brain parenchyma (ie, tissue with relatively high ADC value) improved at high *b* values—the findings noted in this study (Table 5). In this study, larger NEX—five times larger than the routine DWI—was used in acquiring high-*b*-value DWI to maintain the signal intensity-to-noise ratio (9). Thus, the contrast-to-noise ratio for high-*b*-value DWI was five times larger than it should be for equal NEX. For fairer comparison, theoretical contrast-to-noise ratio of high-*b*-value DWI, assuming 2 NEX, was made. This gave the contrast-to-noise ratio of 1.317 for high-*b*-value DWI with 2 NEX—the value still larger than that of routine DWI (ie, 1.112). Further, from the results of theoretical calculation, the *Az* value of high-*b*-value DWI with 2 NEX was found to be larger than that of routine DWI with equal NEX.

In this study, it is likely that the improved contrast and contrast-to-noise ratios have allowed improved accuracy in detection of global cerebral anoxia. In contrast to our findings, the improved contrast of high-*b*-value DWI has failed to improve detection in acute cerebral infarction (15, 16). We speculate that this discrepancy be attributable to the difference in pattern of distribution between the two conditions (1,

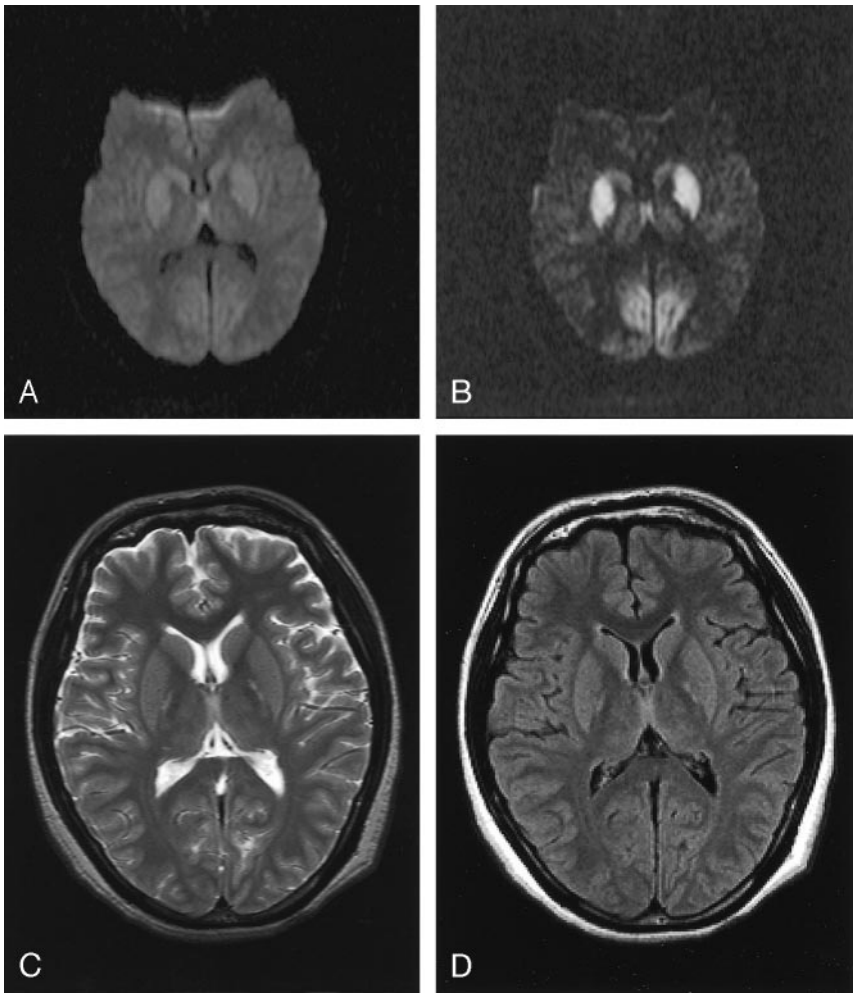

FIG 6. Routine DW image of another patient (*A*). High-*b*-value DW image (*B*). T2-weighted image (*C*). FLAIR image (*D*). The signal intensity abnormalities of bilateral cerebral cortex and deep gray matter are more conspicuous on the high-*b*-value DWI.

TABLE 5: The average contrast and contrast-to-noise ratios

Sequence	Routine DWI	High-b-Value DWI	T2WI	FLAIR Imaging
The average contrast ratio	0.018 ± 0.083	0.121 ± 0.163	0.016 ± 0.097	0.010 ± 0.033
The average contrast-to-noise ratio	1.112 ± 4.600	2.945 ± 5.132	0.863 ± 9.698	0.399 ± 1.697

Note.—Data are presented as mean ± SD.

TABLE 6: T2 values of ROIs

Subjects	ROIs	T2 value (ms)
Patients	Abnormal ROIs	111.3 ± 31.6*
	Normal ROIs	156.1 ± 144.3
	ROIs abnormal only for b-value of 3000 s/mm^2	133.5 ± 49.9
	ROIs abnormal only for b-value of 1000 s/mm^2	87.8 ± 32.1*
Volunteers		138.1 ± 245.5

Note.—Data are represented as mean ± SD. * indicates a statistically significant difference to volunteers ($P < .05$).

17). Acute cerebral infarction involves single vascular territory, whereas in acute period of global cerebral anoxia, widespread involvement of cerebral cortices, deep gray matter, and cerebellum is common. In this study, signal intensity abnormalities were bilateral and symmetrical in all patients (Figs 5, 6). Although unilateral and focal signal intensity abnormality of acute cerebral infarction can be easily recognizable on routine DWI, bilateral and symmetrical signal intensity abnormalities of acute period of global cerebral anoxia may be difficult to detect if the contrast between anoxic tissue and normal tissue is insufficient.

In this study, TE of 190 ms was used in acquiring high-*b*-value DWI. This TE was longer than the reported TEs (<150 ms) for high-*b*-value DWI (7–9, 15, 16, 18–21). The use of long TE is advantageous in suppressing the signal intensity from background brain tissue—valuable for better visualization of hyperintensity, getting rid of the reversal of gray-white matter contrast (Fig 5, 6). The reversal of gray-white matter contrast results from dependence of signal intensity attenuation of tissues on ADC value (7–9).

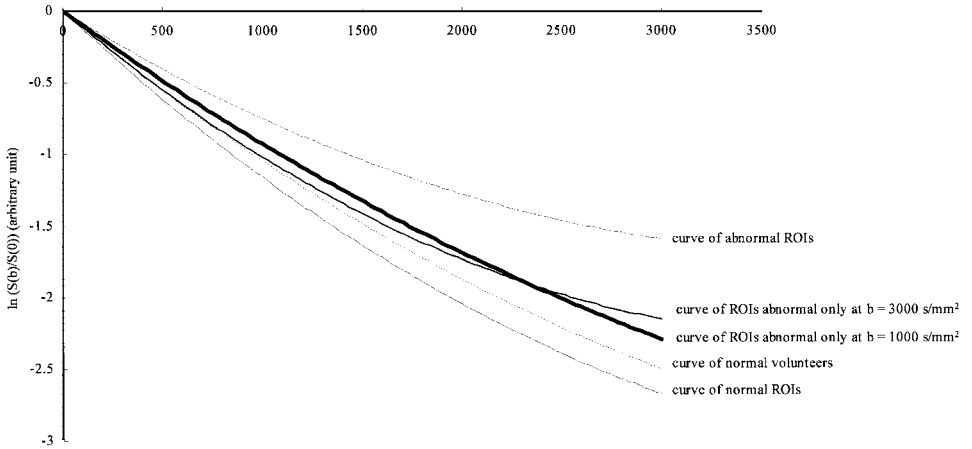

FIG 7. The signal intensity attenuation curves for DWI. The horizontal (*X*) axis represents *b* value (*b*) and the vertical (*Y*) axis represents the logarithmic ratio of signal intensities (ln S[*b*]/*S* [0]).

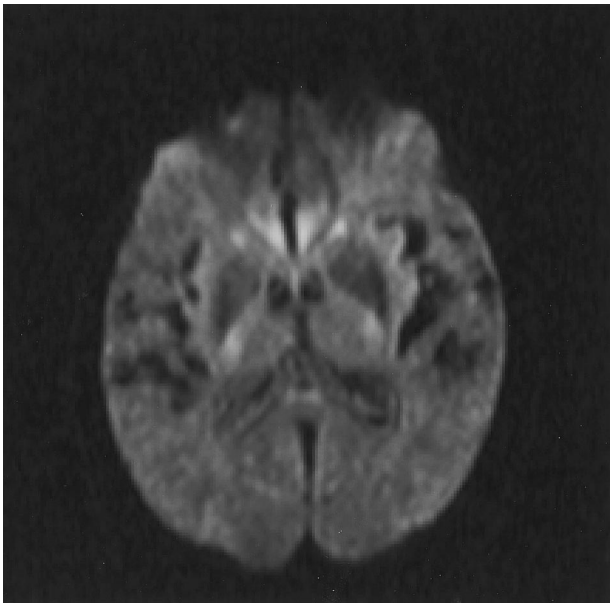

FIG 8. Routine DWI with long TE (190 ms) of a normal subject. Signal intensity from background brain tissue still persists.

This altered pattern of contrast may sometimes lead to erroneous interpretation, if the reader is not accustomed to these images. Besides, hyperintensity of normal white matter can obscure the extent of signal intensity abnormalities, especially in cases with early white matter involvement (10). Compared with high-*b*-value DWI, suppression of background signal intensity is insufficient in routine DWI with the same TE (Fig 8).

Pattern of signal intensity attenuation differed among four groups of regions of interest, defined in this study (Fig 7): (1) abnormal regions of interest, (2) normal regions of interest, (3) regions of interest abnormal only for *b* value of 3000 s/mm^2, and (4) regions of interest abnormal only for *b* value of 1000 s/mm^2. The curve representing abnormal regions of interest (39.6% of total regions of interest) deviated obviously away from other curves. The curve representing normal regions of interest (37.4% of total regions of interest) approached that for normal volunteers. The attenuation curve representing regions of interest abnormal only for *b* value of 3000 s/mm^2 (7.0% of total regions of interest) showed less attenuation at high *b* values. This may indicate relative increase in the fraction of low-mobility water molecules (slow-diffusing component) (7, 8). When the fraction of low-mobility water molecules becomes large, the attenuation curve tends to the case of abnormal regions of interest only for *b* value of 3000 s/mm^2. This may occur when there is relative increase in viscosity of intracellular milieu or macromolecular dissociation (22, 23). The curve representing abnormal regions of interest only for *b* value of 1000 s/mm^2 (15.9% of total regions of interest) approached that of normal volunteers at high *b* values, but deviated upward and away from that of normal volunteers at *b* value of 1000 s/mm^2. Exact underlying pathologic process or etiology to this observation is not understood; however, the finding of T2 shortening in these regions of interest—possibly due to release of free radicals (24, 25)—may implicate.

The optimum b-value, or the b-value at which the maximum contrast-to-noise ratio is achieved, has been considered as best for diagnosis (8, 18). This theoretical optimum *b* value is usually calculated from the ADC values of abnormal and normal regions of interest (18). In this study, the ADC values obtained from the routine DWI gave the optimum *b* value of 1070 ms. If theoretical calculation of contrast-to-noise ratio is made, the *b* value of 3000 s/mm^2 would show a 17% decrease in the ratio, compared with the optimum *b* value. In practice, however, the contrast-to-noise ratio achieved by the high-*b*-value DWI was larger than that of the routine DWI ($b \sim 1070$ ms), even assuming equal NEX. This may reflect that the theoretical contrast-to-noise ratio is a weak function to *b* values. The discrepancy between theoretical and practical contrast-to-noise ratios may owe to T2 shortening in the abnormal regions of interest (Table 6). When T2 of anoxic tissue (abnormal regions of interest) decreases, the contrast between anoxic and normal tissues also decreases. This will demand a

higher *b* value to maximize the contrast-to-noise ratio—the value higher than the theoretical optimum *b* value. Thus, the theoretical optimum *b* value, derived only from the ADC values of abnormal and normal regions of interest, cannot always optimize accuracy in detection. ROC analysis is the most practical method for evaluation of accuracy in detection.

Az, as well as contrast or contrast-to-noise ratios achieved by T2WI and FLAIR imaging, was smaller than the routine DWI or high-*b* value DWI (Figs 4 and 5 and Table 5). Further, even assuming equal NEX, the *Az* value achieved by T2WI or FLAIR imaging was smaller than the two DWI sequences. Although specificity achieved by T2WI or FLAIR imaging was slightly superior to high-*b*-value DWI, these imaging sequences are not comparable to the two DWI sequences in terms of sensitivity and positive and negative predictive values (Table 4). In addition, the acquisition time for T2WI or FLAIR imaging is much longer (ie, 258 seconds for T2WI and 200 seconds for FLAIR imaging) than the DWI sequences with equal NEX. Thus, detection of global cerebral anoxia by T2WI or FLAIR imaging is considered inferior to the DWI sequences. To understand hyperintensity of abnormal regions of interest on T2WI, the property of short and long T2 relaxation components should be taken into account. T2 spectrum of tissue is known to contain short (~20 ms) and long (~110 ms) T2 relaxation components (26, 27). In this study, T2 values were measured by using spin-echo echo-planar T2-weighted images with long TEs (TE = 139 ms and 190 ms). Measurement of T2 values by using long TEs is sensitive to long T2 relaxation component, but insensitive to short T2 relaxation component. Thus, we speculate that the short T2 relaxation component, not observed in our measurement, might be prolonged in these abnormal regions of interest because the long T2 relaxation component was not prolonged.

Early and accurate prediction of neurologic outcome is important for determination of further clinical management (3). Erroneous prediction of poor outcome may deny provision of further life supporting measures, whereas a falsely optimistic prognosis may encourage needless prolongation of life support (3). Early and accurate prediction of neurologic outcome can be achieved through early and accurate detection of global cerebral anoxia (1, 2). It has been suggested that the diffuse cortical hyperintensity on DW images indicates devastating injury and poor neurologic outcome, whereas focal hyperintensity limited to some cortices only is associated with mild hypoxia in which significant neurologic recovery can be expected (2). Our finding of improved accuracy in early detection of global cerebral anoxia by high-*b*-value DWI suggests that high-*b*-value DWI is a useful tool for early detection of global cerebral anoxia.

Conclusion

Our study has shown that the high-*b*-value DWI with long TE improves accuracy in detection of global cerebral anoxia, over other MR imaging sequences, in the acute period. Application of high-*b*-value DWI with long TE in suspected cases of global cerebral anoxia would prove value in early diagnosis and thus early and accurate determination of prognosis and further management.

References

1. Arbalaez A, Castillo M, Mukherji SK. **Diffusion-weighted MR imaging of global cerebral anoxia.** *AJNR Am J Neuroradiol* 1999;20:999–1007
2. Singhal AB, Topcuoglu MA, Koroshetz WJ. **Diffusion MRI in three types of anoxic encephalopathy.** *J Neurol Sci* 2002;196:37–40
3. Hachini-Idrissi S, der Auwera MV, Schiettecatte J, et al. **S-100 protein as early predictor of regaining consciousness after out of hospital cardiac arrest.** *Resuscitation* 2002;53:251–257
4. Booth CM, Boone RH, Tomlinson G, Detsky AS. **Is this patient dead, vegetative, or severely neurologically impaired? Assessing outcome for comatose survivors of cardiac arrest.** *JAMA* 2004;291:870–879
5. Kawahara H, Takeda Y, Tanaka A, et al. **Does diffusion-weighted magnetic resonance imaging enable detection of early ischaemic change following transient cerebral ischemia?** *J Neurol Sci* 2000; 181:73–81
6. Schafer PW, Grant PE, Gonzalez RG. **Diffusion-weighted MR imaging of the brain.** *Radiology* 2000;217:331–345
7. Yoshiura T, Wu O, Zaheer A, et al. **Highly diffusion-sensitized MRI of brain: dissociation of gray and white matter.** *Magn Reson Med* 2001;45:734–740
8. DeLano MC, Cooper TG, Siebert JE, et al. **High-b-value diffusion-weighted MR imaging of adult brain: image contrast and apparent diffusion coefficient map features.** *AJNR Am J Neuroradiol* 2000;21:1830–1836
9. Burdette JH, Durden DD, Elster AD, Yen YF. **High b-value diffusion-weighted MRI of normal brain.** *J Comput Assist Tomogr* 2001;25:515–519
10. Chalela JA, Wolf RL, Maldjian JA, Kasner SE. **MRI identification of early white matter injury in anoxic-ischemic encephalopathy.** *Neurology* 2001;56:481–485
11. Tyler DJ, Moore RJ, Marciani L, Gowland PA. **Rapid and accurate measurement of transverse relaxation times using a single shot multi-echo echo-planar imaging sequence.** *Magn Reson Imaging* 2004;22:1031–1037
12. Abe Y, Yamashita Y, Tang Y, et al. **Calculation of T2 relaxation time from ultrafast single shot sequences for differentiation of liver tumors: comparison of echo-planar, HASTE, and spin-echo sequences.** *Radiat Med* 2000;18:7–14
13. Green DM, Swets JA. *Signal detection theory and psychophysics.* New York: Wiley;1966:96–98
14. Yamashita K, Shiraishi J. **ROC kaiseki no kiso to ouyou.** *Jpn Soc Radiol Technol* 1994;10–21 [in Japanese]
15. Meyer RJ, Gutierrez A, Mock B, et al. **High-b-value diffusion-weighted MR imaging of suspected brain infarction.** *AJNR Am J Neuroradiol* 2000;21:1821–1829
16. Burdette JH, Elster AD. **Diffusion-weighted imaging of cerebral infarctions: are higher B values better?** *J Comput Assist Tomogr* 2002;26:622–627
17. Osborn AG. *Diagnostic neuroradiology.* St. Louis: Mosby;1994: 341–360
18. Pereira RS, Harris AD, Sevick RJ, Frayne R. **Effect of b value on contrast during diffusion-weighted magnetic resonance imaging assessment of acute ischaemic stroke.** *J Magn Reson Imaging* 2002;15:591–596
19. Kubo H, Maeda M, Araki A. **Comparison of apparent diffusion coefficients (ADCs) between two-point and multi-point analyses using high-b-value diffusion MR imaging.** *Jpn J Radiol Technol* 2001;57:634–638
20. Assaf Y, Ben-Bashat D, Chapman J, et al. **High b-value q-space analyzed diffusion-weighted MRI: application to multiple sclerosis.** *Magn Reson Med* 2002;47:115–126
21. Mardor Y, Pfeffer R, Spiegelmann R, et al. **Early detection of response to radiation therapy in patients with brain malignancies using conventional and high b-value diffusion-weighted magnetic resonance imaging.** *J Clin Oncol* 2003;21:1094–1100
22. Neil JJ, Duong TQ, Ackerman JJH. **Evaluation of intracellular diffusion in normal and globally-ischaemic rat brain via ^{133}Cs NMR.** *Magn Reson Med* 1996;35:329–335

23. Schwarcz A, Bogner P, Meric P, et al. **The existence of biexponential signal decay in magnetic resonance diffusion-weighted imaging appears to be independent of compartmentalization.** *Magn Reson Med* 2004;51:278–285
24. Fabian RH, Perez-Polo JR, Kent TA. **Extracellular superoxide concentration increases following cerebral hypoxia but does not affect cerebral blood flow.** *Int J Devl Neurosci* 2004;22:225–230
25. Haimes AB, Zimmerman RD, Morgello S, et al. **MR imaging of brain abscesses.** *AJR Am J Roentgenol* 1989;152:1073–1085
26. Stanisz GJ, Henkelman RM. **Diffusional anisotropy of T2 components in bovine optic nerve.** *Magn Reson Med* 1998;40:405–410
27. Papanikolaou N, Maniatis V, Pappas J, et al. **Biexponential T2 relaxation time analysis of the brain: correlation with magnetization transfer ratio.** *Invest Radiol* 2002;37:363–367